Journal of Food Engineering 341 (2023) 111340

Contents lists available at ScienceDirect

Journal of Food Engineering

journal homepage: www.elsevier.com/locate/jfoodeng

High-resolution thermography and modelling allows for improved characterization of drying sessile single droplets

N.M. Eijkelboom, A.C.M. Swinkels, J. de Ruiter, R.M. Boom, P.F.C. Wilms, M.A.I. Schutyser *

Laboratory of Food Process Engineering, Wageningen University and Research, P.O. Box 17 6700 AA, Wageningen, the Netherlands

ARTICLE INFO

Keywords:
Single droplet drying
Temperature development
Infrared thermography
Modelling
Drying kinetics
Morphology

ABSTRACT

Single droplet drying experiments help to understand droplet drying behavior during spray drying. In this study, high-resolution thermography and high-speed camera monitoring were used to characterize drying behavior of sessile single droplets containing solutes. Selected solutes were maltodextrin with a dextrose equivalent of 6, 21, and 38, whey protein isolate and galacto-oligosaccharide. A heat and mass transfer-based model was developed to describe the drying kinetics of the sessile droplets, assuming ideal shrinkage. This model accurately predicted the drying behavior of the droplets, including the droplet temperature during the constant rate period, the duration of this period, and the final droplet temperature. Remaining differences between measured and predicted droplet temperature are explained by skin formation and subsequent morphological development. Tracking temperature with thermography allows to more accurately follow and understand drying behavior, including morphology development of sessile droplets. It makes it possible to develop better models to translate the obtained insights to spray drying behavior.

1. Introduction

Spray drying is a common process to create a powder from a liquid feed, which is atomized into small droplets and exposed to hot drying air. Due to the large number of droplets, it is not possible to track and study the drying behavior of individual droplets during spray drying (Sadek et al., 2015). To increase the understanding of the drying behavior during spray drying, single droplet drying (SDD) approaches are often used to mimic spray drying at the scale of a single droplet (Boel et al., 2020; Eijkelboom et al., 2022; Fu et al., 2012). The initial droplet size and drying air conditions can be accurately controlled during SDD, which allows the investigation of their influence on drying. Previous SDD studies have, for example, investigated the impact of these parameters on heat-sensitive components, such as enzymes and living bacteria (Schutyser et al., 2012; Siemons et al., 2021), and particle morphology development (Both et al., 2018; Ge, 2005; Sadek et al., 2015; Siemons et al., 2020).

Several different single droplet drying techniques exist, each having their own benefits and limitations. Drying kinetics as assessed by contactless methods, such as free-falling columns, acoustic, aerodynamic or electrodynamic levitation, are not influenced by the presence of a contact area which could influence heat transfer. However, visual observations are more challenging for these contactless methods, as the position of the droplet is not fully static (Eijkelboom et al., 2022). Pendant droplet drying employs static droplets and allows monitoring mass changes as well as visual camera observations. For this technique a small contact area between filament and droplet is present, and relatively large (>500 μm) droplets are required. Although sessile single droplet drying has the largest contact area, it is suitable for visual camera observations and uses smaller droplets (>200 μm) (Eijkelboom et al., 2022). Unfortunately, monitoring drying kinetics during sessile droplet drying is more challenging, as the droplet mass is too small to measure directly with a mass balance. Visual observations can only provide insights into the drying kinetics until the locking point, i.e. the point at which shape deviation is visually observed (Siemons et al., 2020). Another approach to indirectly monitor the drying kinetics is by measuring the droplet temperature (Huelsmann et al., 2020). The droplet temperature stays constant during the constant rate period, increases during the falling rate period and becomes constant again when fully dried. Direct measurement of the droplet temperature also gives insights into the drying kinetics beyond the locking point.

Up till now, the measurement of the temperature of a droplet during drying has been challenging. Invasive methods disturb the droplet's drying behavior (Han et al., 2016), while non-invasive temperature

* Corresponding author.
E-mail address: maarten.schutyser@wur.nl (M.A.I. Schutyser).

https://doi.org/10.1016/j.jfoodeng.2022.111340
Received 7 June 2022; Received in revised form 18 October 2022; Accepted 23 October 2022
Available online 31 October 2022
0260-8774/© 2022 The Author(s). Published by Elsevier Ltd. This is an open access article under the CC BY license (http://creativecommons.org/licenses/by/4.0/).

measurements were not accurate enough for very small droplets (Chen et al., 2016; Duranty et al., 2020; Huelsmann et al., 2020). Infrared thermography has been used to investigate the temperature of drying droplets, but only for droplets of a larger size (1.5–2 mm) (Chen et al., 2016; Duranty et al., 2020; Huelsmann et al., 2020) compared to industrial-scale spray drying, where the droplet sizes are 10–500 μm (Patel and Chen, 2008).

Monitoring the droplet temperature of small drying droplets is important as it influences, together with moisture content, the visco-elastic properties of the material and especially that of the 'skin' with increased solute concentration which is formed at the surface of the drying particle (Siemons et al., 2022). Being able to follow the drying kinetics of a droplet in detail is key to steering particle properties, such as skin properties, which have a profound impact on stickiness and thus indirectly on the agglomeration and fouling during spray drying.

In addition to experimental methods, modelling work has been performed on the drying of droplets to increase the understanding of the drying kinetics. Different types of models have been developed for droplet drying such as multi-physics models (Shamaei et al., 2017; Siemons et al., 2022; Yang et al., 2014) as well as CFD models (Wegener et al., 2014; Woo et al., 2008). The models as developed by Siemons et al. (2022) and Yang et al. (2014) are specifically developed to describe the drying of sessile single droplets. However, these models have not yet been well validated because of the challenges to monitor mass and temperature of these drying droplets in-line (Perdana et al., 2013; Siemons et al., 2022). In sessile droplet drying models the conductive heat transfer was neglected as it was estimated that conductive heat transfer would be limited to 5% of the overall heat transfer or less (Perdana et al., 2013). However, since the impact of conductive heat transfer also depends on the experimental conditions (e.g., droplet size and material of the contact surface), it is important to quantify conductive heat transfer by direct droplet temperature measurement.

The focus of this paper is therefore on the non-invasive analysis of the temperature of a drying sessile single droplet with microscopic infrared thermography and comparing this to modelling results. Drying experiments were performed for different drying matrices (maltodextrin DE6 (MD6), maltodextrin DE21 (MD21), maltodextrin DE38 (MD38), galacto-oligosaccharides and whey protein isolate) at solute concentrations of 20, 30 or 40% (w/w). The droplets had an initial radius of 200 ± 15 μm and were dried with a dry air flow of 0.3 m/s at 60, 75 or 90 °C. Results from this infrared thermography were compared to visual camera observations which were used to track the morphological change and initial drying rate via image analysis. A droplet drying model as developed by Siemons et al. (2022) was extended by including, among others, conductive heat transfer to more accurately predict the experimentally obtained drying rates and temperature development.

2. Materials and methods

2.1. Materials

Polyethylene glycol with an average molecular mass of 400 g/mol (PEG400) was obtained from Sigma Aldrich (St. Louis, MO, USA) and was specifically used to investigate heating of a non-evaporating droplet. Maltodextrins with dextrose equivalence (DE) 6, 21 and 38 were obtained from Roquette Frères (Lestrem, France). Whey protein isolate (WPI) (Nutri Whey™ Isolate R, 90% protein) and galacto-oligosaccharides (GOS) (Vivinal GOS, 69% galacto-oligosaccharides, 23% lactose, 5% glucose and galactose, 3% water) were kindly provided and characterized for their composition by FrieslandCampina (Amersfoort, the Netherlands). The powders were mixed with demineralized water to obtain solutions with a concentration of 20, 30 or 40% (w/w) of solute. Solutions containing WPI were stirred overnight, while the other solutions were stirred for 30 min.

2.2. Viscosity measurements

The viscosities of 20% (w/w) solutions of the different solutes were measured with a strain-controlled rheometer (MCR 301, Anton Paar, Austria). Shear rate sweeps were performed using a double gap geometry (DG26.7/T200/AL, Anton Paar). The shear rate was logarithmically increased from 0.1 to 100 s^{-1}, collecting 30 data points at logarithmically decreasing duration of 300 to 1 s. Subsequently, the procedure was reversed, using a logarithmically decreasing shear rate from 100 to 0.1 s^{-1} taking 30 data points at logarithmically increasing duration of 1–300 s. Samples of different solutes were measured in duplicate; once with and once without the reversed procedure.

2.3. Sessile single droplet drying

The drying of single droplets was performed with the sessile single droplet drying platform as described earlier by Siemons et al. (2020). The droplets were dispensed onto a hydrophobic membrane (Tetratex® ePTFE Polytetrafluoroethylene 3104 membrane, thickness 254 μm, Donaldson Nederland B·V., The Netherlands) using a PipeJet® Nano-Dispenser (BioFluidix, Germany) with ID500-S PipeJet® Pipes (BioFluidix, Germany). BioFluidix Control Software V2.9 (BioFluidix, Germany) was used to control the volume of the droplets (Biofluidix, Germany). The deposited droplets had an initial radius of 200 ± 15 μm, which is within the upper limit of the droplet size range in industrial spray dryers (Patel and Chen, 2008). Droplets were dried in a dry air stream (RH = 1.2%) of 60, 75 or 90 °C with a flow velocity of 0.3 m/s, which corresponds to a surface temperature of 53, 64 or 67 °C respectively. Independent experiments were performed to investigate either the morphological development or the temperature development of a drying droplet.

The morphological development, including particle size and shape, was investigated using a C-VIT high-speed camera (AOS Technologies AG, Switzerland) with a VZMTM 1000 Zoom Imaging Lens (Edmund Optics, Japan). AOS Imaging Studio v4 (AOS Technologies AG, Switzerland) was used to adjust the settings of the camera and to capture the movies. Movies were taken with a frame rate of 500 fps. The lens was set to a zoom of 2.5x and the image format of the camera was set to 360 × 200 pixels. As a light source, a PFBR 150SW MN (CCS Inc., Japan) with a 2″ x 2" back-light module (Vision Light Tech, the Netherlands) was used. The exposure of the camera was set to 2000 μs. The movies were analyzed using a MATLAB (MATLAB R2018b, MathWorks, United States) image analysis script to determine the droplet size until the locking point, based on pixel count. The locking point was manually determined as the first visual observation of spherical shape deviation. The measurements were performed in triplicate. Volume data were extracted from a single representative movie for each experimental condition.

An infrared (IR) camera was used (PI 640 Microscope optics, Optris, Germany) to monitor the droplet temperature. The settings of the camera were controlled with Optris PIX Connect software (Optris, Germany). The camera operated in a temperature range of 0–250 °C and was set to an optical resolution of 640 × 120 pixels, which is paired with a framerate of 125 fps. As the Biot number is clearly lower than 0.4 (Patel and Chen, 2008), the droplet temperature can be assumed uniform. For the temperature measurement, 3 × 3 pixels were taken in the center of the droplet. The infrared measurements were carried out via an AMTIR-1 window (Edmund optics, United States) in the drying tunnel. A calibration curve was created to correct for the emissivity of the material and the transmissivity of the window (Appendix A). For each different condition at least 5 droplets were investigated and representative movies were selected to construct the time-temperature trajectories.

The rate of temperature increase during the falling rate period was determined for the interval where the droplet temperature was in the range of 5 °C above the wet-bulb temperature and 5 °C below its final temperature. The rate of temperature increase is shown as the average

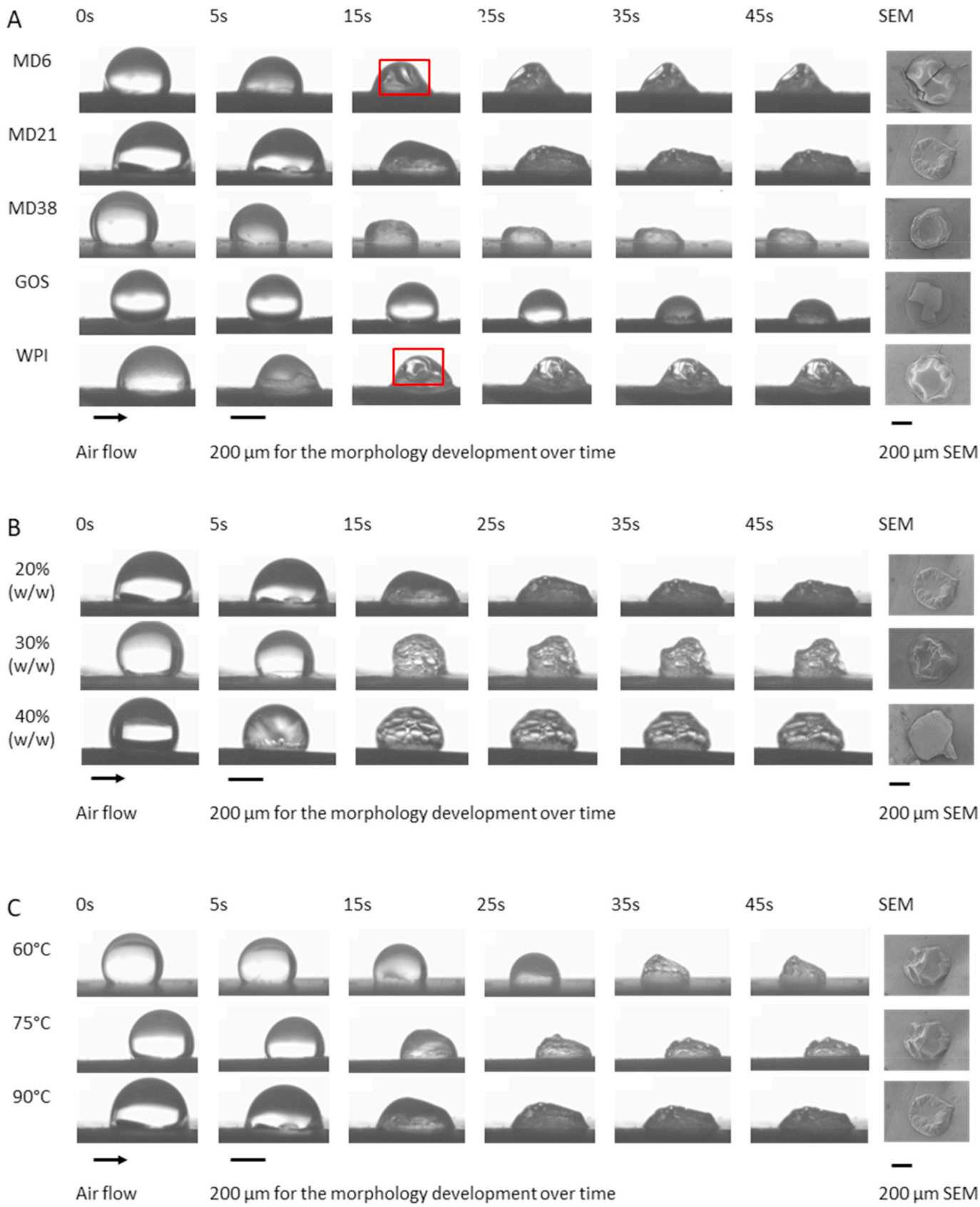

Fig. 1. Morphology development in time for (A) 20% (w/w) solutions of different solutes dried at 90 °C, (B) MD21 solutions of different concentrations dried at 90 °C, and (C) 20% (w/w) MD21 solutions dried at different temperatures. The droplets had an initial radius of 200 ± 15 µm. The rectangles highlight the vacuoles. The droplets were dried with an air flow of 0.3 m/s coming from the left side. A SEM image of the dried particle is included.

value of the replicates investigated under the same conditions. Two-sample t-tests were run in Microsoft Excel (version 16.0, Microsoft Corporation, United States) to determine significant differences ($p < 0.05$) in the rate of temperature increase.

2.4. Single droplet drying modelling

The single droplet drying model used in this research was an effective diffusion drying model, and has been strongly based on the work of Siemons et al. (2022). It is a one-dimensional (1D) model where the droplet is considered to be a spherical cap. The droplet is divided into 20 numerical shells of the same volume and evaporation and heat flux is calculated per shell. An overview of the model parameters and a schematic overview of the model are depicted in Appendix B. The model was implemented in Python (Python 3.6, Python Software Foundation, United States) and Spyder (Spyder 3.7, Spyder Project Contributors, United States) was used to run the model.

The effective diffusive drying model is based on mass and energy transfer theory and makes use of the following equations rewritten in a familiar form of Fick's and Fourier's law:

$$D_t c_w = \nabla \cdot D_m \nabla c_w \tag{1}$$

$$D_t \rho_{eff} c_{p,eff} T = \nabla \cdot \lambda_{eff} \nabla T \tag{2}$$

Where D_t is the time derivative in the Langrangian reference frame (s), c_w the mass concentration of water (kg/m^3), D_m the mutual moisture diffusion (m^2/s), ρ_{eff} the effective density (kg/m^3), $c_{p,eff}$ the effective heat capacity (J/(kg·K)), T the droplet temperature (K), and λ_{eff} the effective heat conductivity (W/(m·K)). The energy and mass balances are solved in spherical coordinates with the cell-centered finite volume scheme, using central differencing, and simple Euler forward time integrations. The initial and boundary conditions applied are:

$$\begin{gathered} c_w(r, t=0) = c_{w,0} \\ T(r, t=0) = T_0 \\ \partial_r c_w(r=0) = 0 \\ \partial_r T(r=0) = 0 \\ -D_m \partial_r c_w(r=R) = J_{evap} \\ -\lambda_{eff} \partial_r T(r=R) = h_{ext}(T - T_{air}) - \left[\Delta H_{evap,0} + \left(c_{p,v} - c_{p,w}\right)(T - T_0)\right] J_{evap} \end{gathered} \tag{3}$$

With r the radial coordinate (m), R the droplet radius (m), $c_{w,0}$ the initial water concentration (kg/m^3), T_0 the reference temperature for the enthalpy of evaporation (273 K), T_{air} the temperature (K) of the bulk air, h_{ext} the external heat transfer coefficient (W/(m^2·K)), $\Delta H_{evap,0}$ the heat of vaporization of water at 273 K (J/kg), and $c_{p,v}$ and $c_{p,w}$ the specific heat of, respectively, vapor and water (J/(kg·K)). The evaporative mass flux J_{evap} (kg/s) equals:

$$\mathrm{J_{evap}} = f_{cap} 4\pi R^2 \beta_{ext} M_w \frac{p_0}{R_{gas} T_{avg}} \ln\left(\frac{p_0 - p_{air}}{p_0 - a_w p_{sat}(T)}\right) \tag{4}$$

With f_{cap} a geometric correction factor used to account for the fact that the droplet is sessile rather than spherical, β_{ext} (m/s) the external mass transfer coefficient, M_w (g/mol) the molecular weight of water, p_0 (Pa) the atmospheric pressure, p_{air} (Pa) the partial dry air pressure, a_w (−) the water activity, and $p_{sat}(T)$ the saturated water vapor pressure (Pa) at the droplet temperature T (K).

The model of Siemons et al. (2022) has been extended by incorporating conductive heat transfer q_c (W) between the droplet and the contact surface:

$$q_c = \frac{A_c(T_{air} - \mathrm{T})}{\frac{L_m}{\lambda_m} + \frac{L_p}{\lambda_p} + \frac{1}{h_{tb}}} \tag{5}$$

Where A_c is the contact area (m^2) between the droplet and the surface. T_{air} and T are the temperature (K) of the air and the droplet respectively.

Table 1
Locking point, moisture content at the locking point, and rate of temperature increase during the falling rate period (temperature between Twb+5 and Tend-5°C) for droplets containing an initial concentration of 20% (w/w) of different solutes, with different letters indicating a significant difference. Solutes are arranged based on their locking point. The viscosity of 20% (w/w) solutions of the solutes measured at 20 °C and a shear rate of 10–100 s^{-1} is also indicated.

Solute	Molecular weight (g/mol)	Viscosity (mPa·s)	Locking point (s)	Moisture content at locking point (% (w/w))	dT/t (°C/s)
WPI	22183[a]	7.91	7.6 ± 0.7	48.6 ± 2.5	1.09 ± 0.11[a]
MD6	3600[b]	11.37	10.4 ± 1.8	42.6 ± 1.1	1.05 ± 0.17[a]
MD21	857[b]	3.20	13.2 ± 1.2	40.2 ± 0.4	1.14 ± 0.13[a]
MD38	474[b]	3.15	14.2 ± 1.6	35.6 ± 0.9	1.42 ± 0.07[b]
GOS	504[c]	2.09	19.2 ± 3.0	29.2 ± 1.8	1.79 ± 0.22[c]

[a] (Deeth and Bansal, 2019).
[b] (Dokic et al., 1998).
[c] (Warmerdam, 2013).

L_m and L_p are the thickness (m) of the membrane and the plate that the membrane is placed on, while λ_m and λ_p are the corresponding thermal conductivities (W/(m·K)). The heat transfer coefficient of the thermal boundary layer is represented by h_{tb} and is set to 1000 W/(m^2·K), a typical value used for air which resulted in a good model fit.

The effective Flory-Huggins excess interaction parameter χ_{eff} (−) was corrected compared to the earlier model:

$$\chi_{eff} = \chi_0 + (\chi_{ws} - \chi_0)(1 - \varphi_w)^2 \tag{6}$$

With χ_0 and χ_{ws} the interaction parameters (−) of water and solute respectively, and φ_w the volume fraction of water (−).

The contact angle θ is one of the factors used to calculate the geometry of the droplet. Whereas the model of Siemons et al. (2022) considered a linear decrease of the contact angle during the constant rate period, this has been modified to align with our observation that the contact line between droplet and surface remains constant. These observations are in-line with our previous studies (Perdana et al., 2013; Siemons et al., 2020). Based on this contact line and the changing height of the droplet, the contact angle was recalculated for every iteration step:

$$\theta = cos^{-1}\left(1 - \frac{H_{drop}}{r_{cap}}\right) * \frac{180}{\pi} \tag{7}$$

With H_{drop} the height of the droplet (m) and r_{cap} the radius of the cap that is not part of the droplet (m), which is half of the contact line diameter.

Some other small adjustments were made compared to the model of Siemons et al. (2022) such as:

- The water content of the droplet is a fraction of the total droplet weight instead of the solute weight.
- The Stefan flux correction for the external evaporative mass flux was not taken into account because of the forced convection caused by the air flow.
- To calculate the diffusivity, the area of a spherical cap is used instead of that of a perfect sphere.

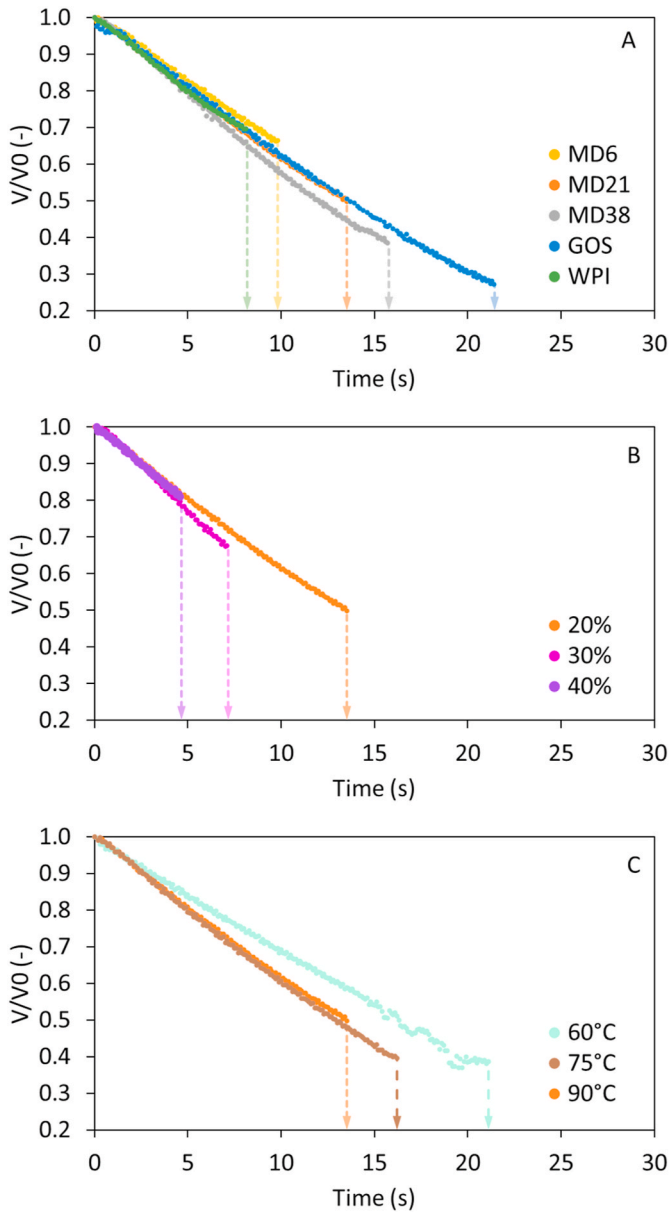

Fig. 2. Volume decrease over time (dots) and locking point (dashes arrows) of drying droplets with an initial radius of 200 ± 15 μm as obtained via the high-speed camera observations for (A) 20% (w/w) solutions of different solutes dried at 90 °C, (B) MD21 solutions of different concentrations dried at 90 °C, and (C) 20% (w/w) MD21 solutions dried at different temperatures.

3. Results and discussion

3.1. Particle morphology development during single droplet drying

During drying of a single droplet, the droplet does not only shrink but also changes in shape. This can be seen in the time series of the morphology of the drying droplets shown in Fig. 1. The change in shape is related to the development of a layer with a high solute concentration at the surface of the droplet, which is referred to as the 'skin'. The mechanical properties of this skin influence the drying behavior of the droplet and the morphology of the dried particle (Both et al., 2020; Sadek et al., 2015; Siemons et al., 2020).

From Fig. 1 it can be seen that the DE value of maltodextrins influences both the morphology and the shrinkage. Generally, the morphology developed earlier, and shrinkage stopped earlier for lower DE values, indicating faster locking (locking point at 10.4 ± 1.8, 13.2 ± 1.2 and 14.2 ± 1.6 s for MD6, MD21 and MD38 respectively (Table 1)). Consequently, the average moisture content of the droplet at the locking point was also higher for lower DE values (moisture content of 42.6 ± 1.1, 40.2 ± 0.4 and 35.6 ± 0.9% (w/w) for MD6, MD21 and MD38 respectively). During the constant rate period, droplets containing different solutes show a similar rate of evaporation (Fig. 2), so an earlier locking point means that less water has evaporated before the locking point is reached.

Also for WPI and GOS a difference in locking point and moisture content at the locking point were observed. The locking point of WPI was at 7.6 ± 0.7 s, while for GOS the locking point was observed at 19.2 ± 3.0 s. The moisture content at the locking point was 48.6 ± 2.5 and 29.2 ± 1.8% (w/w) for WPI and GOS respectively. These observations are in line with the observations of Sugiyama et al. (2006) and Siemons et al. (2020), where droplets containing solutes with a high molecular weight became non-spherical earlier in the drying process. At similar concentrations, solutes with a high molecular weight led to a higher viscosity of the solution (Table 1), leading to an earlier onset of skin formation and emergence of elasticity. When the elastic skin dries further, it will approach the glassy state, resulting in a very high viscosity, and the locking point will be reached (Siemons et al., 2020; Sugiyama et al., 2006). At any temperature, high molecular weight solutes have a glass transition at higher moisture content than low molecular weight solutes, so an earlier locking point is observed (Table 1).

The locking point of a droplet also depends on the initial solute concentration (Fig. 1). The drying rate during the constant rate period is independent of the initial solute content (Fig. 2), but droplets with a higher initial solid content show an earlier locking point (Both et al., 2019). Indeed, the locking points of droplets of 20, 30 and 40% (w/w) solutions of MD21 were observed at 13.2 ± 1.2, 7.8 ± 0.6 and 4.3 ± 0.7 s respectively. The respective average moisture contents at the locking points were 40.2 ± 0.4, 49.7 ± 2.1 and 59.0 ± 0.4% w/w. It is interesting to notice that an earlier locking point comes with a higher moisture content at the locking point, even when this is caused by an increase in the solute concentration. The slower diffusion of solutes within the droplet relative to the evaporation of water creates a solute gradient within the droplet. The water diffusivity in this skin is very strongly dependent on the solute concentration, and therefore this effect dominates the effect of the higher solute and thus the lower amount of water that needs to be evaporated.

The influence of the air temperature on the drying behavior is shown for MD21 in Fig. 1. Droplets dried at a higher air temperature dried faster and showed earlier skin formation, which is in agreement with the observations of Both et al. (2018) and Siemons et al. (2020). Especially the droplets dried at 90 °C showed a higher drying rate than the droplets dried at 60 or 75 °C (Fig. 2). The locking points of droplets of a 20% (w/w) MD21 solution dried at 60, 75 and 90 °C were observed at 20.1 ± 1.1, 16.2 ± 1.4 and 13.2 ± 1.2 s respectively. The droplets dried at 60 and 75 °C show similar moisture contents at the locking point (36.9 ± 3.6 and 36.1 ± 2.4% (w/w)), while the moisture content of a droplet dried at 90 °C is a bit higher (40.2 ± 0.4% (w/w)). These observations are in the same order of magnitude as the observation of Lin and Chen (2004) and Siemons et al. (2020). They observed that the drying air temperature had only little effect on the normalized droplet radius at the locking point.

3.2. Droplet temperature

While visual camera observations provide insight into the drying rate until the locking point, the droplets become too irregularly shaped after the locking point, to enable the estimation of the droplet's volume. Droplet temperature measurements can however be used to assess the drying kinetics throughout the full drying period. High-resolution thermography was used to measure the temperature of the droplets during drying and an example of the images obtained during the

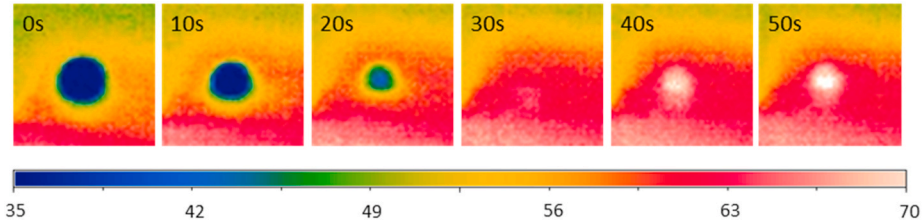

Fig. 3. Infrared thermography images over time for a drying droplet of a 20% MD21 solution with an initial radius of 200 ± 15 μm, dried with air of 90 °C and a flow rate of 0.3 m/s. A color bar with reference temperatures for the droplet is also provided.

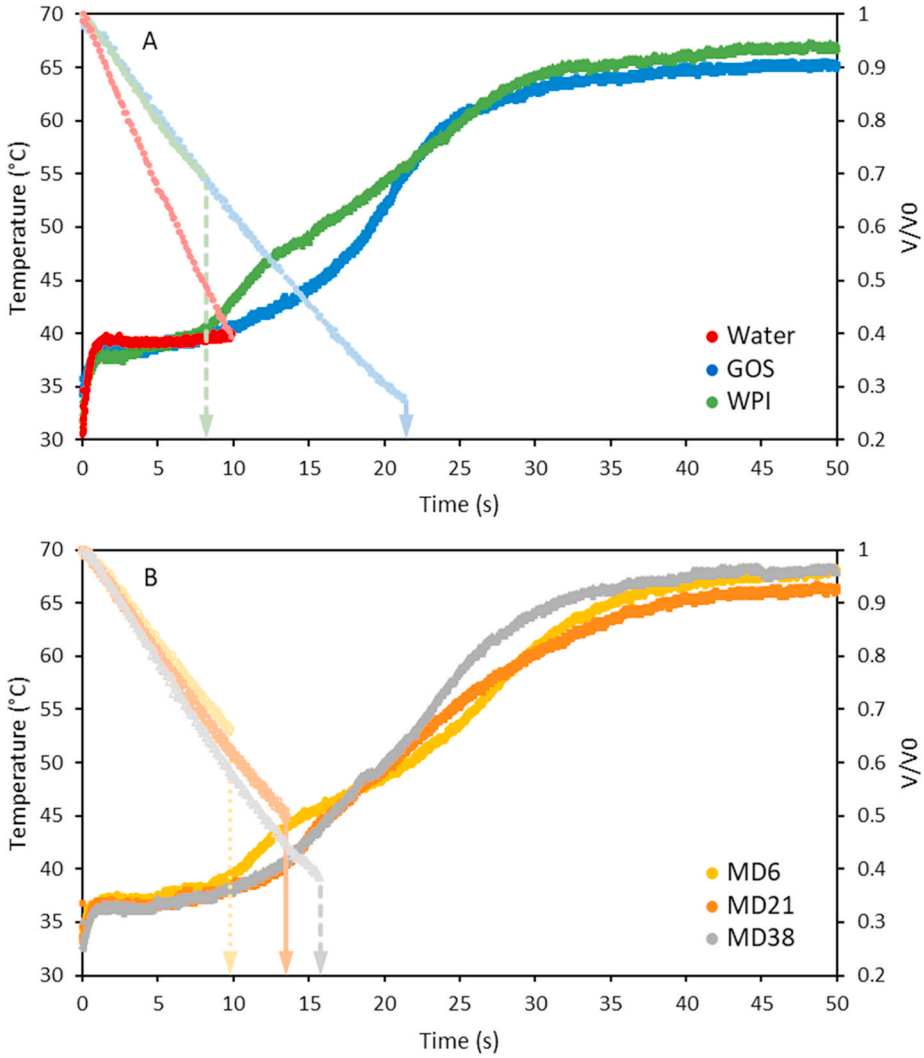

Fig. 4. Time-temperature and time-volume curves of droplets dried at 90 °C with an air flow rate of 0.3 m/s. Temperature (bright dots), volume (pale dots) and the visually observed locking point (dashed arrows, Table 1) are indicated. Because droplet volume measurement is inaccurate after the locking point, measurements stop at this point.

measurements is shown in Fig. 3. Fig. 4 shows the temperature development of drying droplets containing different solutes.

At the start of the drying process, during the initial heating period, the droplet temperature increases from room temperature to a constant temperature close to the wet-bulb temperature (Fig. 4), although it may deviate somewhat due to the thermal contact between droplet and supporting plateau. The constant rate period sets in, during which the moisture content of the droplet is high and gas-phase transfer is limiting (Anandharamakrishnan and Padma Ishwarya, 2015; Boel et al., 2020). This is why this initial constant droplet temperature is independent of the nature and concentration of the solute (Fig. 4).

While water evaporates from the surface of the droplet, the concentration of solutes at the surface increases. The increased solute concentration hinders water evaporation, which is in line with the lower rate of volume decrease, and hence lower evaporation rate, that is observed for solute-containing droplets as compared to pure water (Fig. 4) (Fu et al., 2013). The increase in solute concentration close to the surface eventually leads to the formation of a skin at the surface of the droplet. The diffusivity of water drops very sharply with decreasing moisture content, and the highly-concentrated skin therefore limits the transport of water to the surface. Hence, the evaporation rate drops, and temperature of the droplet increases and the falling rate period begins

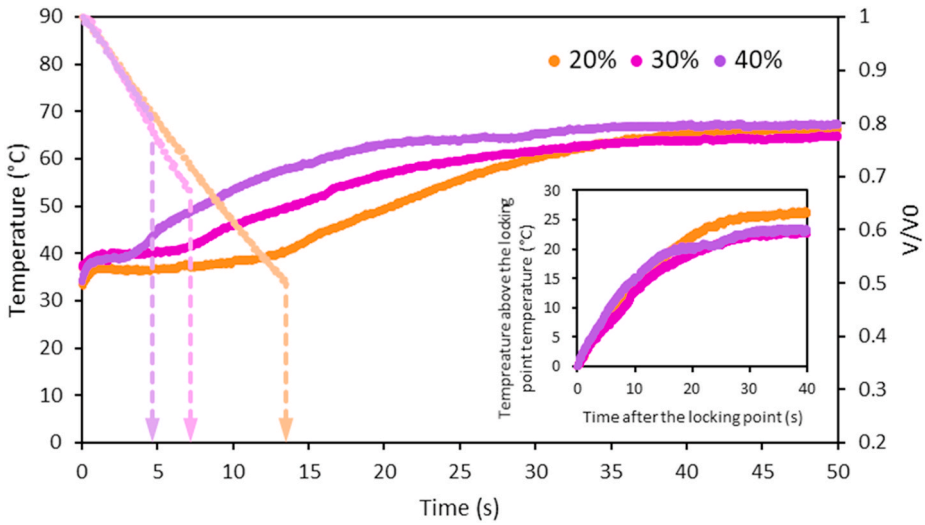

Fig. 5. Droplets of MD21 solutions of different initial concentrations were dried at 90 °C with a flow rate of 0.3 m/s. Temperature (big bright dots), volume (small pale dots) and the locking point (dashed arrow), are indicated. Because droplet volume measurement is inaccurate after the locking point, measurements stop at this point. The insert shows the temperature increase after the locking point.

(Leniger and Beverloo, 1975).

For WPI, MD6 and MD21, the moment at which the droplet temperature starts to increase is almost identical to the visually observed locking point time (Fig. 4). This is due to the formation of the skin at the surface of the droplet resulting in the start of morphological changes as well as the hindrance of evaporative cooling (Boel et al., 2020; Both et al., 2019). For GOS and MD38, there is no clear correlation between the end of the constant rate period and the visually observed locking point time (Fig. 4). The GOS used in this study consist of a mixture of galacto-oligosaccharides with different degrees of polymerization (DP), with 95% of the oligosaccharides having a DP between 2 and 5. In addition, the powder contains 23% of lactose. For small compounds, such as MD38 and the lactose and low DP galacto-oligosaccharides present in GOS, the solute diffusivity is higher than for sugars with a higher DP value. This means that small compounds can better diffuse from the skin towards the bulk of the droplet, thereby not contributing as strongly to the formation of a dense skin at the surface. The onset of the morphological changes will therefore be delayed (Siemons et al., 2021).

The rate at which the temperature of the droplet increases, depends on the solute that is present and more specifically on its molecular weight (Table 1). The rate of temperature increase is lowest for WPI and low DE maltodextrins, higher for MD38 and the highest for GOS (Table 1). Because of the higher solute diffusivity, solute accumulation at the surface is slower, and hence the skin formation takes longer for low molecular weight compounds. This is in line with the later locking point of the MD38 and GOS droplets. As it takes more time before a skin is formed, more evaporation has taken place and the droplets will be smaller at the locking point. These smaller droplets have a larger surface area to volume ratio, which promotes faster heating (Mondragón et al., 2013). In addition, the droplets have a lower moisture content at their locking point, which results in a lower specific heat capacity. Consequently, the evaporation rate, and hence the level of evaporative cooling, is lower, causing a more rapid temperature increase.

The temperature increase after locking is more irregular for MD6 and WPI droplets than for MD21, MD38 and GOS droplets (Fig. 4). While the temperature increase for MD21, MD38 and GOS is rather constant over time, MD6 and WPI show a plateau in their temperature increase. This is linked to differences in morphological development; the MD6 and WPI droplets form vacuoles while the MD21, MD38 and GOS droplets become wrinkled (Fig. 1). Droplets that show vacuole formation have a more elastic skin, which can withstand deformation. When this elastic skin becomes rigid, further shrinkage of the droplet is prevented, but evaporation continues through the skin. This creates a local pressure minimum, and a vacuole forms inside the droplet. The vacuole results in an inward elastic stress, leading to rupture of the skin. This hole results in a sudden increase in the contact area with the environment, resulting in an increase in evaporation (Bouman et al., 2016). The enhanced evaporative cooling reduces the droplet's temperature increase, resulting in a small plateau in the droplet temperature development (Appendix C, Video 1). Therefore, the rate of temperature increase in this period after locking was considered to be a good indicator for the morphological development of a drying droplet.

The temperature of the drying particle increases until it reaches the temperature of its surroundings (Anandharamakrishnan and Padma Ishwarya, 2015; Boel et al., 2020). In the case of sessile SDD, this final temperature is equal to the temperature of the substrate that the dried particle is in contact with. This is in line with the experimental observations, where the particles reach a final temperature close to the substrate temperature of 67 °C when applying a hot air flow of 90 °C (Fig. 4). The temperature of the substrate is lower than the air temperature due to heat loss via conduction.

Droplets of different initial concentrations of MD21 were dried to investigate the effects of the initial solute concentration on the temperature development of a drying droplet (Fig. 5). For the three different MD21 concentrations investigated, the end of the constant rate period aligns well with the locking point (Fig. 5). A locking point requires a minimum concentration of solute on the interface, to be in the region of dramatic reduction of the water diffusivity (Both et al., 2018; Siemons et al., 2020; Tran et al., 2016). At higher concentrations, this is reached earlier.

There is no significant difference in rate of temperature increase for the droplets with different initial MD21 concentrations (1.14 ± 0.13, 0.93 ± 0.13 and 1.06 ± 0.27 °C/s for the 20, 30 and 40% (w/w) solutions respectively). Gouaou et al. (2019) indicated that droplets with different initial solid contents in the decreasing flux period showed similar evaporative fluxes at a similar moisture content. Despite different initial concentrations, locking point formation starts when a specific, high concentration of MD21 is reached at the surface of the droplet. This concentration is independent of the initial solute concentration, meaning that droplets of different initial MD21 concentrations are expected to have similar moisture contents at the surface of the droplet when skin formation starts. The mechanical properties of the skin will therefore be similar, which is also observed by the similar

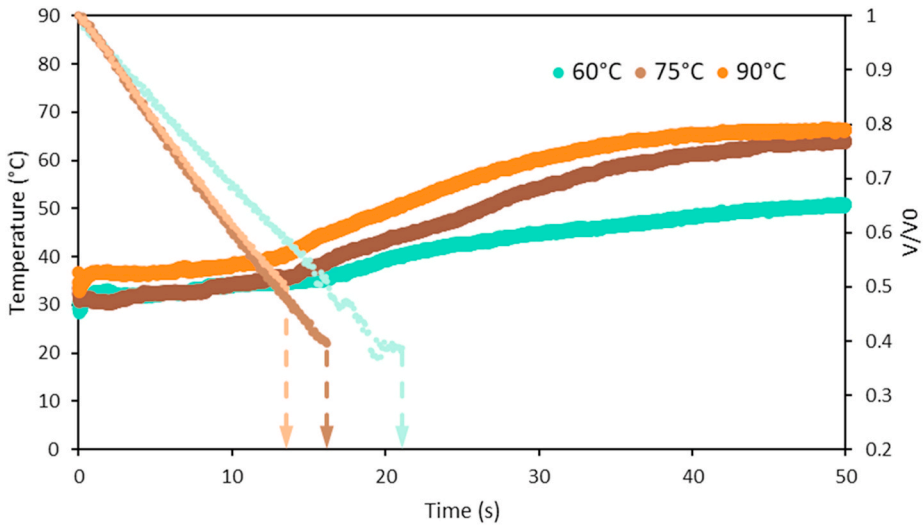

Fig. 6. Droplets of MD21 solutions of 20% (w/w) were dried at different temperatures with a flow rate of 0.3 m/s. Temperature (big bright dots), volume (small pale dots) and the locking point (dashed arrow), are indicated. Because droplet volume measurement is inaccurate after the locking point, measurements stop at this point.

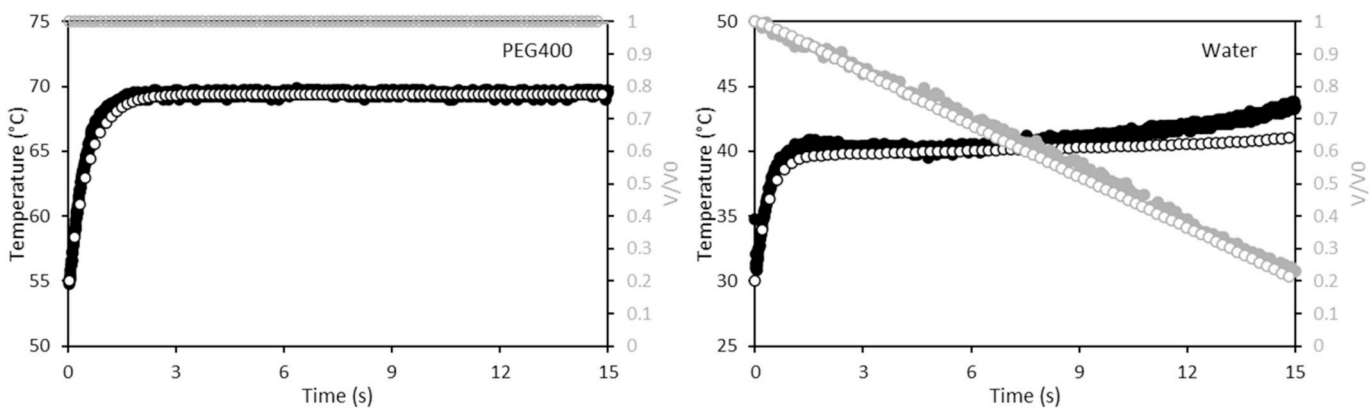

Fig. 7. Temperature increase and volume decrease of a PEG400 and water droplet with an initial radius of 200 ± 15 μm dried at 90 °C, with the experimental droplet temperature (●), the droplet temperature as predicted by the model (○), the experimental droplet volume (●) and the model predictions regarding the droplet volume (○).

morphological development after the locking point (Fig. 1). This indicates that, after the locking point, the rate of evaporative cooling is independent of the initial solute concentration, resulting in the same rate of temperature increase (Fig. 5).

To investigate the influence of the drying air temperature on the drying kinetics of a sessile single droplet, droplets of a 20% (w/w) MD21 solution were dried at different temperatures (Fig. 6). For the three different temperatures investigated (60, 75 and 90 °C), drying at a lower temperature results in a later locking point, which is in line with the observations of Both et al. (2018). At a lower air temperature, the driving force for evaporation is lower and hence the rate of evaporation is lower. As a result, the accumulation of solute in the skin is less extreme and the locking point comes later. The expected differences in the evaporation rate are, however, not large, especially at higher temperatures. Although the shrinkage of the droplet is the slowest at an air temperature of 60 °C, the shrinkage rates observed for the droplets dried at 75 °C and 90 °C are very similar. This is because the difference in heat transfer between 75 °C and 90 °C is not as large as between 60 °C and 75 °C, especially because of the limited difference of the temperature of the contact surface at these air temperatures (64 and 67 °C, respectively), which contributes to the heat supply to the droplet.

3.3. Model development

During preliminary experiments, it was found that sessile single droplets of, among others, maltodextrin solutions have a higher initial temperature than the wet-bulb temperature. This was assumed to be caused by conductive heat transfer from the surface on which the droplet was deposited. To estimate the rate of this heat transfer, the heating of a non-evaporating polyethylene glycol (PEG400) droplet and the evaporation of a water droplet without solute were studied. Next to adding a conductive heat transfer term in the model (Equation (3)), the heat transfer via the air was modified to correct for the non-ideal spherical geometry of the droplet. This was done through the external heat transfer coefficient β_{ext} (m/s), which was originally based on a perfectly spherical geometry, to obtain a good description for heating of a PEG400 droplet and an evaporating water droplet (Fig. 7). A good fit was obtained when the external mass transfer coefficient was corrected by $\beta_{ext,sessile} = 0.4 * \beta_{ext,sphere}$. The calculations then show that for the water droplet, 40% of the heat entering the droplet originates from conductive heat transfer. This relatively large contribution of the conductive heat transfer distinguishes a drying sessile single droplet from a droplet drying in a spray dryer. However, if the model that describes the drying behavior of a drying sessile droplet accurately predicts both conductive and convective heat transfer, the model results can be

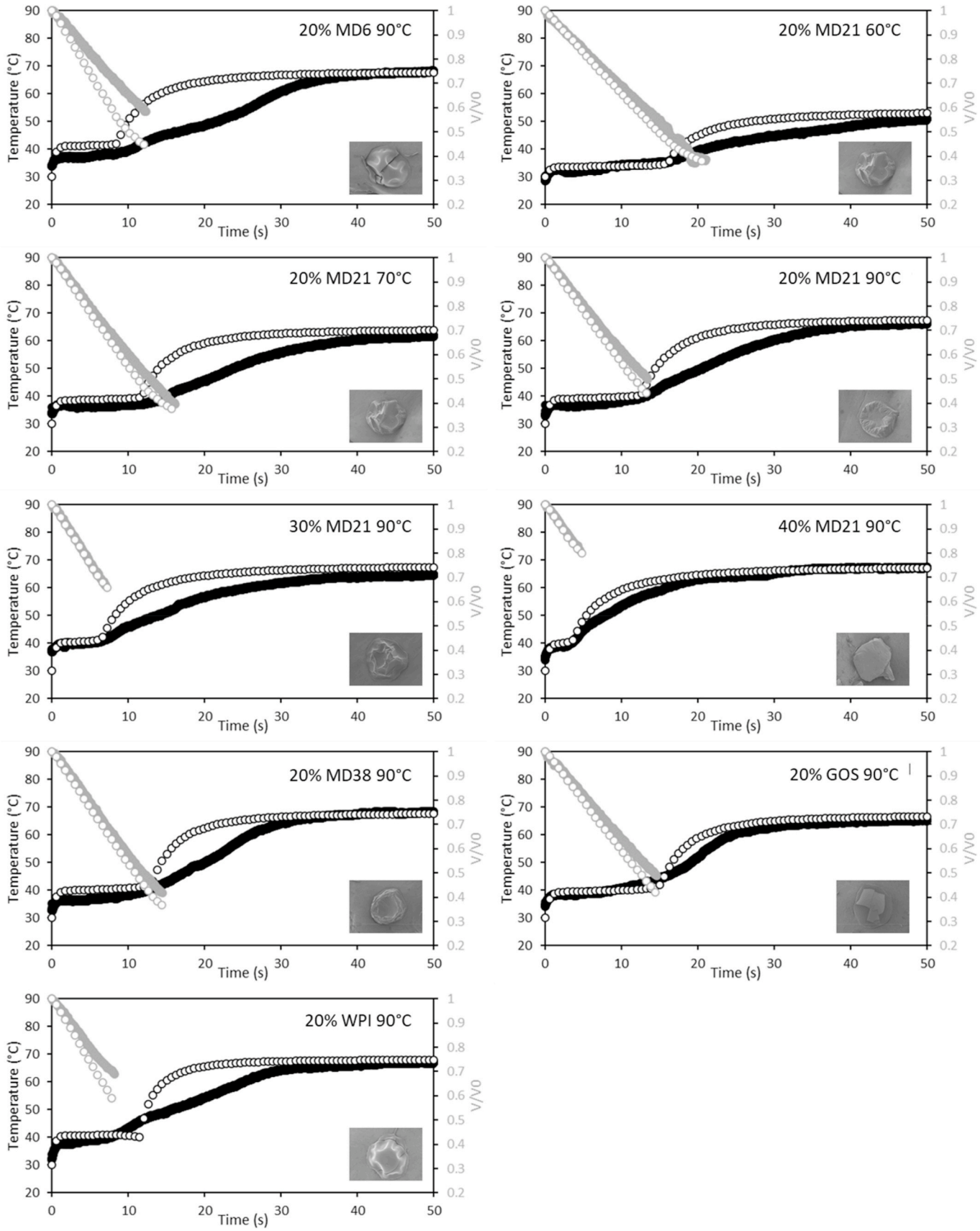

Fig. 8. Temperature increase, volume decrease and final particle morphology of droplets of different solutions with an initial radius of 200 ± 15 μm dried at different air temperatures at a flow of 0.3 m/s. The graphs show the experimental droplet temperature as determined with the IR camera (●), the droplet temperature as predicted by the model (○), the experimental droplet volume as determined with the visual camera observations (●) and the model predictions regarding the droplet volume (○).

extrapolated to free flying droplets that rely on convective heat transfer.

The improved sessile single droplet drying model (open symbols) was compared to the experimental measurements of the different solutions (closed symbols). The droplet temperature is shown for the full drying period, while the volume decrease of the droplet is only shown until the locking point (Fig. 8). The reason for this is that from the locking point onwards the droplet becomes irregularly shaped (e.g., vacuole formation or wrinkling), which is not described by the one-dimensional drying model that is used. Until the locking point, the model predictions related to the volume decrease generally show a good match with the experimental results (Fig. 8). This is especially true for the droplets of a 40% MD21 solution and a 20% GOS solution, which show smooth particles with limited dents. Larger deviations in volume prediction, with lower predicted volume decrease compared to the experimental values, are observed for the droplets of a 20% DE6 and a 20% WPI solution (Fig. 8), which are the droplets showing vacuole formation (Fig. 8). It is unclear what causes these larger deviations, but it might be related to the earlier formation of a thin skin, hindering evaporation slightly but still allowing isotropic shrinkage.

The model adequately predicts the initial droplet temperature during the constant rate period, the duration of this period, as well as the final droplet temperature. During the time that the droplet temperature increases from the initial constant temperature to the final temperature, there are some deviations between the model predictions and the experimental results, with the model predicting a higher temperature than observed experimentally, which is related to the development of an irregular morphology. As was observed in Table 1, Fig. 4 and Appendix C Video 1, the rate of temperature increase depends on the morphological changes that occur during the drying process. The difference between the model and measurements can thus be considered as a fingerprint for morphology development: the difference between model and experiment is larger if the morphology is less spherical or contains a vacuole. The direct prediction of the irregularities would require a multidimensional model which was out of the scope of this study.

4. Conclusions

Single droplet drying studies are key to obtain insights into the impact of drying conditions on the drying kinetics of a droplet. While visual camera observations have been used to gain insights into the drying kinetics of drying sessile single droplets until the locking point, they failed until now to obtain relevant information further in the drying process (Siemons et al., 2020). High-resolution thermography is used within this research to obtain more relevant information during the entire drying process.

Droplets of 20% (w/w) solutions of MD6, MD21 and MD38, GOS and WPI were dried at 90 °C. For MD21 the influence of initial solute content was further investigated by drying droplets with an initial concentration of 30 and 40% (w/w). The impact of drying air temperature was examined by drying droplets of a 20% (w/w) MD21 solution at 60 and 75 °C. Both visual camera observations, as well as IR measurements, showed that the drying kinetics during the constant rate period depends on the drying air temperature, but not on the composition of the droplet. The duration of the constant rate period was found to be compound-specific and related to the morphological locking point of the droplet. The high concentration of solute at the surface leads to development of a skin, which is responsible for morphological changes as well as for the hindering evaporation, thereby inhibiting the droplet from staying at the wet-bulb temperature.

Although the IR measurements cannot be directly used to determine the particle morphology, the time-temperature results can serve as an indirect measure for morphological development of the droplet. Droplets that form a vacuole during drying show a more irregular temperature increase, with a plateau of the droplet's temperature when the vacuole is formed. The formation of a vacuole can also be observed with the sessile single droplet drying model. Assuming morphological changes to be the main cause for the deviations between the predicted and experimentally observed droplet volume, these deviations can be considered a fingerprint for morphology development. A further understanding of these deviations could lead to insights into the drying behavior of a droplet. The combination of high-resolution thermography and an effective-diffusion-based model could thus provide valuable information to predict droplet surface properties during the entire drying process, not just until the locking point. This is an important step to steer spray drying processes to obtain powders with desired surface properties. Because of the profound impact of surface properties on stickiness and thus indirectly on agglomeration, this will help to control agglomeration and to prevent fouling in a spray dryer.

Credit authorship contribution statements

N.M. Eijkelboom: Conceptualization, Methodology, Validation, Formal analysis, Investigation, Visualization, Writing – original draft, Writing – review & editing. **A.C.M. Swinkels**: Methodology, Investigation. **J. de Ruiter**: Conceptualization, Supervision, Writing – review & editing. **R.M. Boom**: Supervision, Writing – review & editing. **P.F.C. Wilms**: Supervision, Writing – review & editing. **M.A.I. Schutyser**: Conceptualization, Supervision, Writing – review & editing, Funding acquisition.

Declaration of interest

All authors declare no potential conflict of interest related to the presented work.

Data availability

Data will be made available on request.

Acknowledgements

This work is an Institute for Sustainable Process Technology (ISPT) project, i.e. StAggloP (Project number: DR-50-15). Partners in this project are Corbion, Danone, DSM, FrieslandCampina, University of Hohenheim, Wageningen University & Research and ISPT. Special thanks to FrieslandCampina for providing the WPI and GOS. This project is co-funded with subsidy from the Topsector Energy by the Dutch Ministry of Economic Affairs and Climate Policy. We also would like to thank Julia Veser and Ruud van der Sman for discussions about the drying model and its implementation.

Appendix A

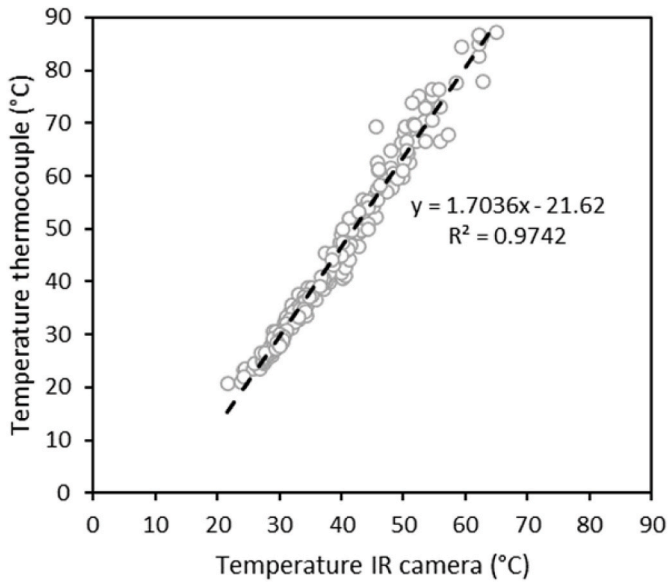

Fig. 9. Calibration curve as used for the infrared temperature measurements, with the dots showing the experimental measurement points and the dashed line the calibration curve. Measurements were performed with a larger volume of water or 40% MD21 solution.

Appendix B

Table 1
Nomenclature as used in this paper.

Abbreviations	
DE	Dextrose equivalence
GOS	Galacto-oligosaccharides
IR	Infrared
MDX	Maltodextrin with dextrose equivalence X
SDD	Single droplet drying
WPI	Whey protein isolate
Symbols	
A_c	Contact area between droplet and surface (m^2)
a_w	Water activity (-)
$c_{p,eff}$	Effective heat capacity (J/(kg·K))
$c_{p,v}$	Specific heat of vapor (J/(kg·K))
$c_{p,w}$	Specific heat of water (J/(kg·K))
C_w	Mass concentration of water (kg/m^3)
$C_{w,0}$	Initial water concentration (kg/m^3)
D_m	Mutual moisture diffusion (m^2/s)
D_t	Time derivative in the Langrangian reference frame (s)
f_{cap}	Geometric correction factor (-)
H_{drop}	Height of the droplet (m)
h_{ext}	External heat transfer coefficient ($W/(m^2 \cdot K)$)
h_{tb}	Heat transfer coefficient thermal boundary layer ($W/(m^2 \cdot K)$)
J_{evap}	Evaporative mass flux (kg/s)
L_m	Thickness of the membrane (m)
L_p	Thickness of the plate (m)
M_w	Molecular weight of water (g/mol)
p_0	Atmospheric pressure (Pa)
p_{air}	Partial dry air pressure (Pa)
$p_{sat}(T)$	Saturated water vapor pressure at the droplet temperature T (Pa)
q_c	Conductive heat transfer (W)
R	Droplet radius (m)
r	Radial coordinate (m)
r_{cap}	Radius of the cap that is not part of the droplet (m)
T	Droplet temperature (K)
T_0	Reference temperature for the enthalpy of evaporation (273 K)
T_{air}	Temperature of the bulk air (K)
β_{ext}	External mass transfer coefficient (m/s)
$\Delta H_{evap,0}$	Heat of vaporization of water at 273 K (J/kg)
Θ	Contact angle (°)
λ_{eff}	Effective heat conductivity (W/(m·K))
λ_m	Thermal conductivity of the membrane (W/(m·K))

(*continued on next page*)

Table 1 (*continued*)

Abbreviations	
λ_p	Thermal conductivity of the plate (W/(m·K))
ρ_{eff}	Effective density (kg/m^3)
φ_w	Volume fraction of water (-)
χ_0	Interaction parameter of water (-)
χ_{eff}	Effective Flory-Huggins excess interaction parameter (-)
χ_{ws}	Interaction parameter of solute (-)

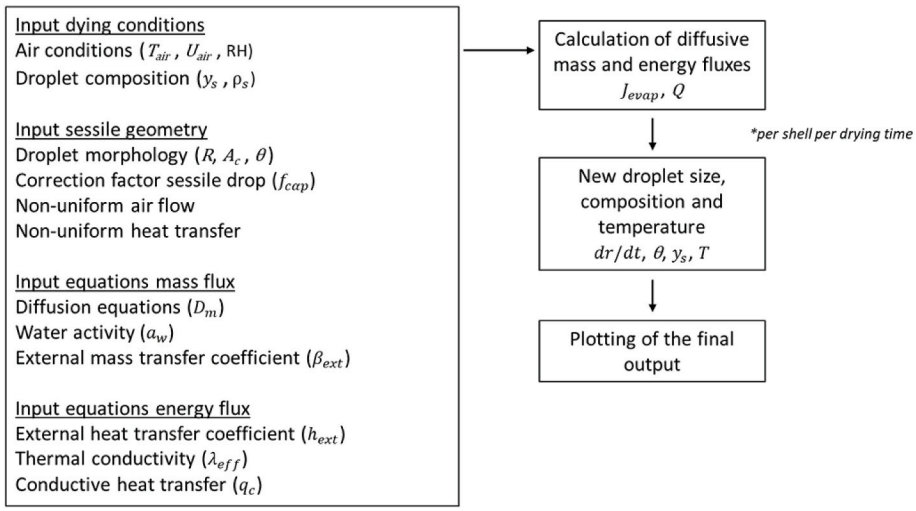

Fig. 10. Schematic diagram of the sessile single droplet drying model, adapted from Siemons et al. (2021).

Appendix C. Supplementary data

Supplementary data to this article can be found online at https://doi.org/10.1016/j.jfoodeng.2022.111340.

References

Anandharamakrishnan, C., Padma Ishwarya, S., 2015. Spray Drying Techniques for Food Ingredient Encapsulation.

Boel, E., Koekoekx, R., Dedroog, S., Babkin, I., Vetrano, M.R., Clasen, C., Van den Mooter, G., 2020. Unraveling particle formation: from single droplet drying to spray drying and electrospraying. Pharmaceutics 12 (7), 1–58. https://doi.org/10.3390/pharmaceutics12070625. MDPI AG.

Both, E.M., Karlina, A.M., Boom, R.M., Schutyser, M.A.I., 2018. Morphology development during sessile single droplet drying of mixed maltodextrin and whey protein solutions. Food Hydrocolloids 75, 202–210. https://doi.org/10.1016/j.foodhyd.2017.08.022.

Both, E.M., Siemons, I., Boom, R.M., Schutyser, M.A.I., 2019. The role of viscosity in morphology development during single droplet drying. Food Hydrocolloids 94, 510–518. https://doi.org/10.1016/j.foodhyd.2019.03.023.

Both, E.M., Tersteeg, S.M.B., Boom, R.M., Schutyser, M.A.I., 2020. Drying kinetics and viscoelastic properties of concentrated thin films as a model system for spray drying. Colloids Surf. A Physicochem. Eng. Asp. 585, 124075 https://doi.org/10.1016/j.colsurfa.2019.124075.

Bouman, J., Venema, P., De Vries, R.J., Van Der Linden, E., Schutyser, M.A.I., 2016. Hole and vacuole formation during drying of sessile whey protein droplets. Food Res. Int. 84, 128–135. https://doi.org/10.1016/j.foodres.2016.03.027.

Chen, P., Toubal, M., Carlier, J., Harmand, S., Nongaillard, B., Bigerelle, M., 2016. Evaporation of binary sessile drops: infrared and acoustic methods to track alcohol concentration at the interface and on the surface. Langmuir 32, 9836–9845. https://doi.org/10.1021/acs.langmuir.6b02564.

Deeth, H., Bansal, N., 2019. Whey Proteins: An Overview. In: *Whey proteins: from milk to medicine*. Academic Press, pp. 1–50. https://doi.org/10.1016/B978-0-12-812124-5.00001-1.

Dokic, P., Jakovljevic, J., Dokic-Baucal, L., 1998. Molecular characteristics of maltodextrins and rheological behaviour of diluted and concentrated solutions. Colloids and Surfaces A: Physicochemical and Engineering Aspects 141, 435–440. https://doi.org/10.1016/S0927-7757(97)00118-0.

Duranty, E.R., Mccardle, H., Reichert, W.M., Davis, J.H., 2020. Acoustic levitation and infrared thermography: a sound approach to studying droplet evaporation. This Journal Is Cite This: Chem. Commun. 56, 4224. https://doi.org/10.1039/c9cc09856a.

Eijkelboom, N.M., Boven, A. P. Van, Siemons, I., Wilms, P.F.C., Boom, R.M., Kohlus, R., Schutyser, M.A.I., 2022. Particle structure development during spray drying from a single droplet to pilot-scale perspective. J. Food Eng. 337 https://doi.org/10.1016/j.jfoodeng.2022.111222.

Fu, N., Woo, M.W., Chen, X.D., 2012. Single droplet drying technique to study drying kinetics measurement and particle functionality: a review. Dry. Technol. 30 (15), 1771–1785. https://doi.org/10.1080/07373937.2012.708002.

Fu, N., Woo, M.W., Selomulya, C., Chen, X.D., 2013. Shrinkage behaviour of skim milk droplets during air drying. J. Food Eng. 116 (1), 37–44. https://doi.org/10.1016/j.jfoodeng.2012.11.005.

Ge, Y., 2005. 3D Numerical Study on Droplet-Solid Collisions in the Leidenfrost Regime. The Ohio State University.

Gouaou, I., Shamaei, S., Koutchoukali, M.S., Bouhelassa, M., Tsotsas, E., Kharaghani, A., 2019. Impact of operating conditions on a single droplet and spray drying of hydroxypropylated pea starch: process performance and final powder properties. Asia Pac. J. Chem. Eng. 14 (1), e2268. https://doi.org/10.1002/apj.2268.

Han, K., Song, G., Ma, X., Yang, B., 2016. An experimental and theoretical study of the effect of suspended thermocouple on the single droplet evaporation. Appl. Therm. Eng. 10, 568–575. https://doi.org/10.1016/j.applthermaleng.2015.12.022.

Huelsmann, R., Esper, G.J., Kohlus, R., 2020. Using an acoustic levitator to investigate the drying kinetics and solids forming process of individual droplets during spray drying. Prog. Agric. Eng. Sci. 16 (1), 41–49. https://doi.org/10.1556/446.2020.00011.

Leniger, H.A., Beverloo, W.A., 1975. Food Process Engineering. D. Reidel.

Lin, S.X.Q., Chen, X.D., 2004. Changes in milk droplet diameter during drying under constant drying conditions investigated using the glass-filament method. Food Bioprod. Process. 82 (3), 213–218. https://doi.org/10.1205/fbio.82.3.213.44178.

Mondragón, R., Juliá, J.E., Hernández, L., Jarque, J.C., 2013. Influence of particle size on the drying kinetics of single droplets containing mixtures of nanoparticles and microparticles: modeling and pilot-scale validation. Dry. Technol. 31 (7), 759–768. https://doi.org/10.1080/07373937.2012.757233.

Patel, K.C., Chen, X.D., 2008. Surface-center temperature differences within milk droplets during convective drying and drying-based Biot number analysis. AIChE J. 54 (12), 3273–3290. https://doi.org/10.1002/aic.11608.

Perdana, J., Fox, M.B., Schutyser, M.A.I., Boom, R.M., 2013. Mimicking spray drying by drying of single droplets deposited on a flat surface. Food Bioprocess Technol. 6 (4), 964–977. https://doi.org/10.1007/s11947-011-0767-4.

Sadek, C., Schuck, P., Fallourd, Y., Pradeau, N., Le Floch-Fouéré, C., Jeantet, R., 2015. Drying of a single droplet to investigate process–structure–function relationships: a

review. Dairy Sci. Technol. 95 (6), 771–794. https://doi.org/10.1007/s13594-014-0186-1.

Schutyser, M.A.I., Perdana, J., Boom, R.M., 2012. Single droplet drying for optimal spray drying of enzymes and probiotics. Trends Food Sci. Technol. 27 (2), 73–82. https://doi.org/10.1016/j.tifs.2012.05.006.

Shamaei, S., Seiiedlou, S.S., Aghbashlo, M., Valizadeh, H., 2017. Mathematical modeling of drying behavior of single emulsion droplets containing functional oil. Food Bioprod. Process. 101, 100–109. https://doi.org/10.1016/j.fbp.2016.10.012.

Siemons, I., Politiek, R.G.A., Boom, R.M., van der Sman, R.G.M., Schutyser, M.A.I., 2020. Dextrose equivalence of maltodextrins determines particle morphology development during single sessile droplet drying. Food Res. Int. 131 https://doi.org/10.1016/j.foodres.2020.108988.

Siemons, I., Vaessen, E.M.J., Oosterbaan Van Peski, S.E., Boom, R.M., Schutyser, M.A.I., 2021. Protective effect of carrier matrices on survival of Lactobacillus plantarum WCFS1 during single droplet drying explained by particle morphology development. J. Food Eng. 292, 110263 https://doi.org/10.1016/j.jfoodeng.2020.110263.

Siemons, I., Veser, J., Boom, R.M., Schutyser, M.A.I., van der Sman, R.G.M., 2022. Rheological behaviour of concentrated maltodextrins describes skin formation and morphology development during droplet drying. Food Hydrocolloids 126, 107442. https://doi.org/10.1016/j.foodhyd.2021.107442.

Sugiyama, Y., Larsen, R.J., Kim, J.-W., Weitz, D.A., 2006. Buckling and crumpling of drying droplets of Colloid−Polymer suspensions. Langmuir 22 (14), 6024–6030. https://doi.org/10.1021/LA053419H.

Tran, T.T.H., Avila-Acevedo, J.G., Tsotsas, E., 2016. Enhanced methods for experimental investigation of single droplet drying kinetics and application to lactose/water. Dry. Technol. 34 (10), 1185–1195. https://doi.org/10.1080/07373937.2015.1100202.

Warmerdam, A., 2013. Synthesis of galacto-oligosaccharides with β-galactosidases.

Wegener, M., Paul, N., Kraume, M., 2014. Fluid dynamics and mass transfer at single droplets in liquid/liquid systems. Int. J. Heat Mass Tran. 71, 475–495. https://doi.org/10.1016/J.IJHEATMASSTRANSFER.2013.12.024.

Woo, M.W., Daud, W.R.W., Mujumdar, A.S., Talib, M.Z.M., Hua, W.Z., Tasirin, S.M., 2008. Comparative study of droplet drying models for CFD modelling. Chem. Eng. Res. Des. 86 (9), 1038–1048. https://doi.org/10.1016/j.cherd.2008.04.003.

Yang, K., Hong, F., Cheng, P., 2014. A fully coupled numerical simulation of sessile droplet evaporation using Arbitrary Lagrangian-Eulerian formulation. Int. J. Heat Mass Tran. 70, 409–420. https://doi.org/10.1016/j.ijheatmasstransfer.2013.11.017.